

Article

Weldability of Molybdenum–Rhenium Alloy Based on a Single-Mode Fiber Laser

Liang-Liang Zhang ^{1,*}, Lin-Jie Zhang ² and Qing-Jie Yang ²

¹ College of Metallurgical Engineering, Xi'an University of Architecture and Technology, Xi'an 710055, China

² State Key Laboratory of Mechanical Behavior for Materials, Xi'an Jiaotong University, Xi'an 710049, China; zhanglingjie@mail.xjtu.edu.cn (L.-J.Z.); yqj1528389401@stu.xjtu.edu.cn (Q.-J.Y.)

* Correspondence: llzhang@xauat.edu.cn; Tel.: +86-137-0898-4539

Abstract: Due to its high thermal conductivity and favorable machinability, molybdenum–rhenium (Mo–Re) alloys have huge prospects in the field of high-temperature heat pipes. However, the weldability of Mo–Re alloys has not yet been systematically investigated. Based on an orthogonal test, the influence law of the single-mode fiber laser welding parameters on the weld profile and the mechanical properties of the joints was studied. Furthermore, the existence mode and the distribution law of Re in the fusion zone (FZ) were explored using X-ray photoelectron spectrometer (XPS) and the electron backscattered diffraction (EBSD) system. The results showed that weld penetration and width are most significantly influenced by power, and that these increased with increasing power. The tensile strength of the Mo–Re alloy joints reached 250 MPa, and no obvious hardening was found in the FZ. Re in the FZ also appeared as ReO₂, ReO₃, and ReC, apart from the atomic state.

Keywords: molybdenum–rhenium alloy; single-mode fiber laser; X-ray photoelectron spectrometer; electron backscattered diffraction



Citation: Zhang, L.-L.; Zhang, L.-J.; Yang, Q.-J. Weldability of Molybdenum–Rhenium Alloy Based on a Single-Mode Fiber Laser. *Metals* **2022**, *12*, 841. <https://doi.org/10.3390/met12050841>

Academic Editors:
Aleksander Lisiecki and
Leu-Wen Tsay

Received: 21 March 2022

Accepted: 29 April 2022

Published: 13 May 2022

Publisher's Note: MDPI stays neutral with regard to jurisdictional claims in published maps and institutional affiliations.



Copyright: © 2022 by the authors. Licensee MDPI, Basel, Switzerland. This article is an open access article distributed under the terms and conditions of the Creative Commons Attribution (CC BY) license (<https://creativecommons.org/licenses/by/4.0/>).

1. Introduction

Molybdenum (Mo) is highly applicable for the manufacture of ultra-high-temperature liquid metal heat pipes, which is considered a key part of the ultra-high-temperature passive heat transport system of miniature nuclear reactors [1–3]. However, the cold/hot workability of Mo is poor [4,5]. Due to the softening effect of rhenium [6–8], the strength of the Mo–Re alloy is enhanced, while the ductile–brittle transition temperature (DBTT) is reduced. However, the strength and ductility of the fusion welding joints of the Mo–Re alloy is still very low [9].

The embrittlement of the joints can be ascribed to three aspects: Firstly, the formation of Re-rich phases lowers the distribution uniformity of Re, then decreases the uniformity of microstructures and mechanical properties of the FZ, thus leading to brittleness of the joints [10]. Secondly, the segregation of impurity elements such as oxygen (O) on the grain boundary surface in the FZ decreases the bonding strength of the grain boundary while increases its brittleness. A study [11] on the lap joint of the Mo–Re alloy (50Mo–50Re) produced by powder metallurgy with a thickness of 0.13 mm, welded using a Nd:YAG laser, showed that there were numerous dark compounds in the grains and at grain boundaries in the FZ. The composition analysis indicated that O content in the dark compounds is as high as 15 at.%. Thirdly, grain coarsening decreases the grain boundary bonding strength while increasing the embrittlement of the FZ [12–14]. The main reason for this is that grain coarsening reduces the area of the grain boundaries; the segregation degree of the impurity elements at the grain boundary is increased when the contents of impurity elements such as O are fixed. Moreover, the higher the contents of O and N on the grain boundary surface, the lower the bonding strength [12,15] and the higher the brittleness [16,17].

Porosity can also decrease the strength of joints [8,18–20]. The gas in the porosities of the FZ is mainly sourced from residual gas in the microvoids of the BM manufactured

via powder metallurgy, and the protective atmosphere during the welding. Morito [21] found that numerous pores are distributed on the surface of the grain boundary during electron-beam welding of the Mo–13Re alloy; Liu et al. [11] suggested that pronounced porous defects appear on the cross section of the joint during laser welding of the lap joint of the Mo–50Re alloy, and the pore size reaches 15~20% of the thickness of the BM.

The above aspects are regarded as the main factors that cause the reduction in strength and ductility of welded joints for the Mo–Re alloy. However, one or several factors probably play a role with regard to specific welding methods and specific types of Mo–Re alloys. The higher the Re content in the Mo–Re alloy, the better the weldability of the alloy and the lower the loss of strength and the ductility of the joints. Due to the Re content being quite low in the BM of the Mo–5Re alloy, and a part of the Re being burned during the welding, the content of Re in the FZ is lower than that in the BM. Whether or not quite a low Re content can still strengthen the joints needs to be studied. Thus, it is necessary to analyze the content, existence mode, and distribution of Re in the FZ and heat-affected zone (HAZ) of the welding joints to clarify the influencing mechanism of Re behaviors on the strength of joints. In this study, a single-mode fiber laser with a smaller diameter and better quality compared to the traditional laser beams was employed to weld the Mo–Re alloy, in order to decrease the heat input.

2. Materials and Methods

2.1. Materials

Mo–5Re sheets manufactured via powder metallurgy with a thickness of 2 mm were used, in which the Re content reached 5 wt.%. The contents of the other elements are displayed in Table 1. For the convenience of the subsequent test, Mo–Re alloy sheets with a thickness of 2 mm were separately ground into those with thicknesses of 1 mm and 0.5 mm. The specific dimensions are shown in Figure 1.

Table 1. Relative contents of various elements in the Mo–5Re sheets.

Elements	Mo	Re	K	Na	Sn	Ca	Fe	Mn
Contents (wt.%)	Bal.	5	≤0.002	≤0.002	≤0.001	≤0.0002	≤0.0055	≤0.0015

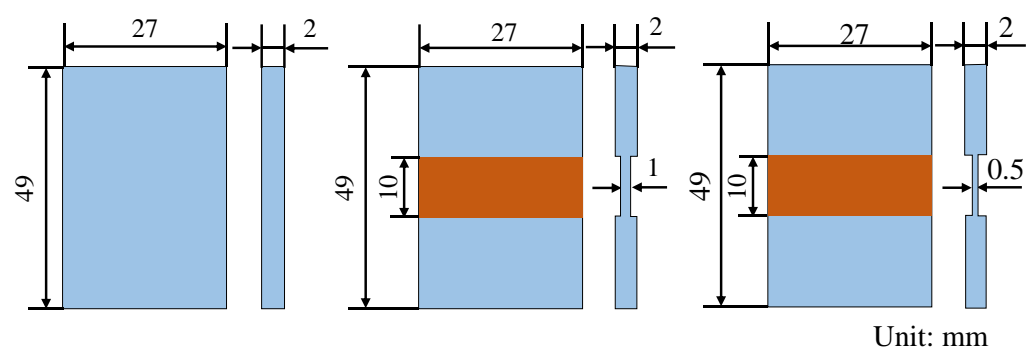


Figure 1. The specific dimensions of Mo–5Re sheets with thicknesses of 2 mm, 1 mm, and 0.5 mm.

2.2. Laser Beam Welding System

The laser beam welding system mainly consisted of a SPI Qube–LT single-mode fiber laser (SPI, Hamble, UK), an ABB IRB–4600 motorman (ABB, Beijing, China), preheating equipment (made by the authors), and a gas protection device (made by the authors), as shown in Figure 2. The maximum power of the SPI laser was 2 kW; the minimum spot diameter was 50 μm ; the wavelength was 1075 ± 2 nm. During welding, the samples were cleaned with acetone and preplaced into the gas protection device in Figure 2c; afterwards, the equipment was covered and argon was injected for 1 min; finally, the Mo–Re sheet was welded using a laser.

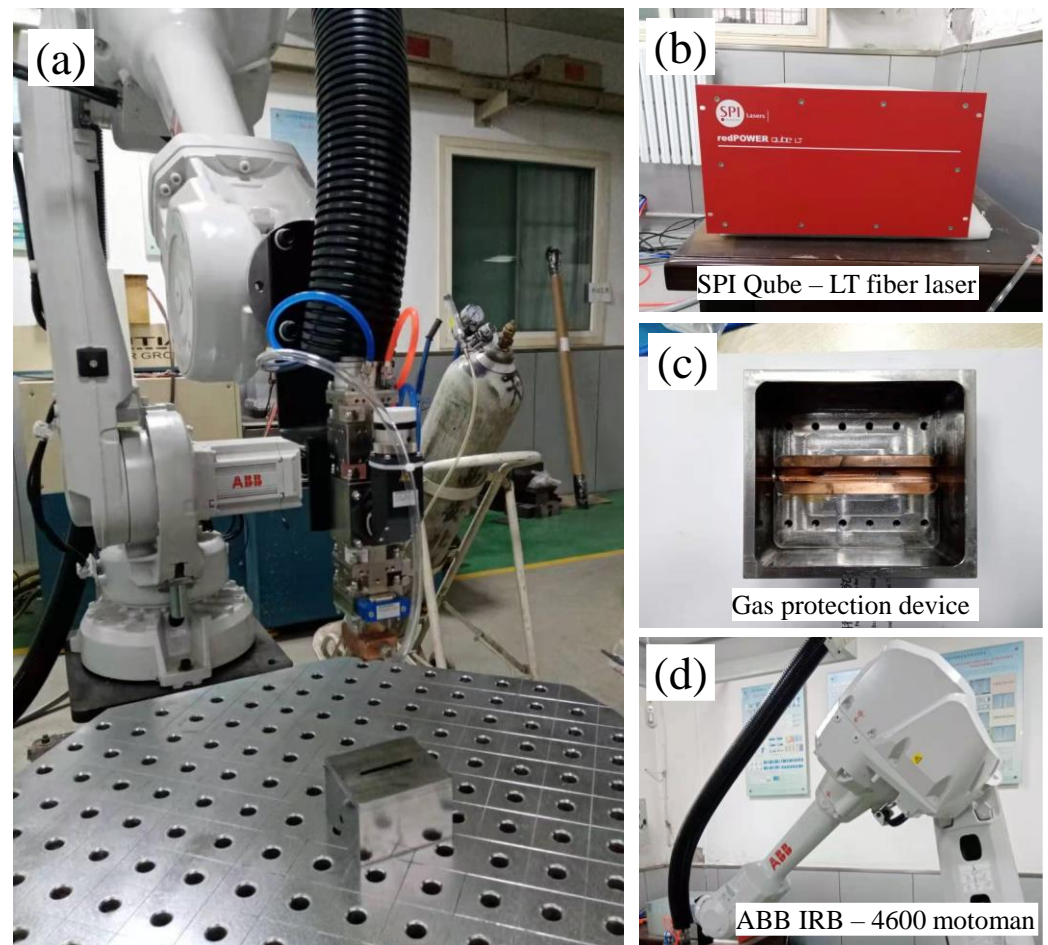


Figure 2. (a) The single-mode fiber laser welding system; (b) SPI fiber laser; (c) gas protection device; (d) ABB motorman.

2.3. Orthogonal Test Schemes for Mo–5Re Sheets with Different Thicknesses

The optimizing of orthogonal experimental parameters is first based on welded depth. Firstly, the parameters in Table 2 were selected for the orthogonal experiments on a 2 mm thick Mo-Re alloy plate to analyze the effect of the different power, welding speed and defocusing amount on the penetration depth. So as to optimize the parameters used in subsequent penetration welding. Secondly, the parameters with penetration depth greater than 1mm in Table 2 were selected as the basis for the optimization of the next step of the penetration welding parameters (Table 3). Lastly, welding experiments were carried out with the parameters in Table 3, and tensile tests were conducted. Taking the tensile strength of the joint as an index, the influence of different power, welding speed and defocus quantity on the strength of the joint was analyzed.

Table 2. Three-factor and four-level (L16 (34)) orthogonal test schemes for laser welding of Mo–5Re sheets with a thickness of 2 mm.

Test Number	Defocusing Amount (mm)	Power (kW)	Welding Speed (m/min)
1 (2) #	1	1.4	0.3
2 (2) #	1	1.6	0.4
3 (2) #	1	1.8	0.5
4 (2) #	1	2	0.6
5 (2) #	0.5	1.4	0.4
6 (2) #	0.5	1.6	0.3
7 (2) #	0.5	1.8	0.6
8 (2) #	0.5	2	0.5
9 (2) #	0	1.4	0.5
10 (2) #	0	1.6	0.6
11 (2) #	0	1.8	0.3
12 (2) #	0	2	0.4
13 (2) #	−0.5	1.4	0.6
14 (2) #	−0.5	1.6	0.5
15 (2) #	−0.05	1.8	0.4
16 (2) #	−0.50	2	0.3

Table 3. Three-factor and three-level (L8 (33)) orthogonal test schemes for laser welding of Mo–5Re sheets with a thickness of 0.5 mm.

Test Number	Defocusing Amount (mm)	Power (kW)	Welding Speed (m/min)
1 (0.5) #	1	1.4	2
2 (0.5) #	1	1.7	3
3 (0.5) #	1	2	4
4 (0.5) #	0.5	1.4	3
5 (0.5) #	0.5	1.7	4
6 (0.5) #	0.5	2	2
7 (0.5) #	0	1.7	2
8 (0.5) #	0	2	3
9 (0.5) #	0	1.4	4

2.4. Mechanical Testing and Microstructure Analysis

The tensile test of the joints was performed using an Instron testing machine (WDS-20, Jinan HengXu Testing Machine Technology Co., Ltd., Jinan, China) with a rate of 0.1 mm/min; moreover, the tensile fracture was observed using a Zeiss Gemini SEM 500 scanning electron microscope (SEM, Zeiss, Jena, Germany). The Vickers hardness of the BM, HAZ, and FZ in the cross sections of the joints were tested using a Vickers microhardness tester (QHV-1000SPTA, Laizhou Weiyi Co., Ltd., Laizhou, China), under a load of 50 gf and a holding time of 15 s.

A mixed solution of 10% NaOH (Shanghai Aladdin Biochemical Technology Co., Ltd., Shanghai, China) and 10% $K_3[Fe(CN)_6]$ (Shanghai Aladdin Biochemical Technology Co., Ltd., Shanghai, China) with a volume ratio of 1:1 was used to corrode the cross sections of the joints for 10 s to prepare the metallographic samples. The microstructures of the cross sections of the joints were observed using a Nikon Eclipse MA200 optical microscope (Nikon, Suzhou, China). In addition, the Oxford electron backscattered diffraction (EBSD, Oxford Instruments, Shanghai, China) system was utilized to detect the phase compositions and their distribution in the FZ of the cross sections. The position of the sample used in the EBSD experiment was the cross section of the weld. First, the samples were polished with sandpaper of #100–#2000, respectively. Then, the sample was polished to a mirror state on a polishing machine (Laizhou Weiyi Co., Ltd., Laizhou, China). Finally, the sample was polished through electrolytic polishing technology, in which the electrolytic polishing solution was a sulfuric acid and ethanol mixture (a volume ratio of 1:7). The polishing voltage was 18 V, the current was 0.6 A, and the polishing time was 3 s.

The chemical valences of the Mo and Re elements in the FZ and HAZ of the cross sections of the joints were analyzed using a Thermo Fisher ESCALAB Xi+ X-ray photoelectron spectrometer (XPS, ThermoFisher Scientific, New York, NY, USA). During the test, the beam spot diameter equaled 300 μm , and the Pass Energy 20 eV analyzer mode and Al-K α X-ray source were employed, with a test step of 0.1 eV. The spectral peak tested was corrected by C 1s (284.6 eV). To avoid oxidation, the surfaces of the cross sections of the joints to be measured were cleaned for 30 s with Ar ion beams at 1000 eV before the test.

3. Results

3.1. The Influence Law of Welding Parameters on Morphologies and Sizes of Weld Beads

Table 4 shows the statistical results of the penetrations of the joints of the Mo–Re sheets with a thickness of 2 mm, during a three-factor and four-level orthogonal test. The values k1~k5 represent the mean values of the penetrations under different factors at the same level, which reflect the influences of a factor at different levels of the penetration; R stands for the range of penetrations obtained under each factor at different levels, which reflect the influences of different factors on the penetration. As shown in the Table 4, the penetration was the lowest (0.16 mm) at a defocusing amount of 1 mm, a power of 1.4 kW, and a welding speed of 0.3 m/min; the maximum penetration (1.57 mm) was found at a defocusing amount of -0.5 mm, a power of 2 kW, and a welding speed of 0.3 m/min. By further analyzing the R values corresponding to the different factors, it was found that the factors were displayed in a descending order as power, welding speed, and defocusing amount in terms of R. A larger R value corresponding to a factor indicates a greater influence of the factor on the penetration. Therefore, the power and the defocusing amount separately delivered the most and least significant influences on the penetration.

Table 4. Penetrations of the laser-welded Mo–Re sheets with a thickness of 2 mm, during a three-factor and four-level orthogonal test.

Test Number	Defocusing Amount (mm)	Power (kW)	Welding Speed (m/min)	Penetration (mm)
1 (2) #	1	1.4	0.3	0.16
2 (2) #	1	1.6	0.4	0.58
3 (2) #	1	1.8	0.5	0.98
4 (2) #	1	2	0.6	0.96
5 (2) #	0.5	1.4	0.4	0.22
6 (2) #	0.5	1.6	0.3	0.60
7 (2) #	0.5	1.8	0.6	0.46
8 (2) #	0.5	2	0.5	1.11
9 (2) #	0	1.4	0.5	0.31
10 (2) #	0	1.6	0.6	0.23
11 (2) #	0	1.8	0.3	0.70
12 (2) #	0	2	0.4	1.06
13 (2) #	-0.5	1.4	0.6	0.32
14 (2) #	-0.5	1.6	0.5	0.23
15 (2) #	-0.5	1.8	0.4	0.71
16 (2) #	-0.5	2	0.3	1.57
k1	0.670	0.251	0.757	-
k2	0.596	0.412	0.642	-
k3	0.574	0.713	0.659	-
k4	0.708	1.171	0.883	-
R	0.134	0.920	0.241	-

Furthermore, the effects of the defocusing amount, power, and welding speed on the penetration were attained by comparing the relationships of different factors and levels with k indexes, as shown in Figure 3. The penetration reduced at first, and then rose with an increasing defocusing amount (Figure 3a). Both the negative and positive defocusing amounts were in favor of growing the penetration; the penetration also always increased with an increase of laser power (Figure 3b). Moreover, the higher the power, the larger the growth rate of the penetration (as evinced by the rising slope of the curve in Figure 3c); as the welding speed increased, the penetration decreased; however, the penetration at the welding speed of 0.5 m/min was slightly larger than that at 0.4 m/min.

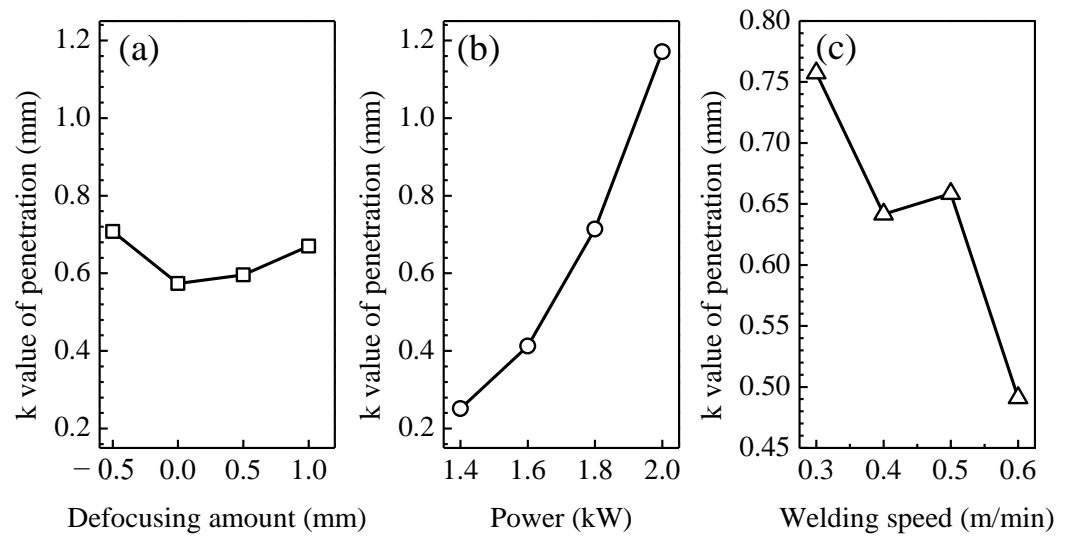


Figure 3. Relationships between (a) the defocusing amount, (b) power, and (c) welding speed with the penetration of the laser-welded joints of Mo–Re sheets with a thickness of 2 mm.

Table 5 displays the statistical results of the width of the Mo–Re joints with a thickness of 2 mm during a three-factor and four-level orthogonal test (here, the width of weld on the upper surface was measured). The values k_1 – k_5 represent the mean values of the weld width obtained under different factors at the same level; R stands for the range of the weld width obtained under each factor at different levels. At first, the weld width was the lowest (0.7 mm) at a defocusing amount of 0 mm, a power of 1.4 kW, and a welding speed of 0.5 m/min; the maximum weld width (2.0 mm) occurred at a defocusing amount of -0.5 mm, a power of 2 kW, and a welding speed of 0.3 m/min. By further analyzing the R values corresponding to different factors, it was found that the factors were shown in a descending order as laser power, welding speed, and defocusing amount, in terms of R . This means that the power and the defocusing amount separately presented the most and least pronounced influences on the weld width.

Table 5. The width of the laser-welded Mo–Re sheets with a thickness of 2 mm during a three-factor and four-level orthogonal test.

Test Number	Defocusing Amount (mm)	Power (kW)	Welding Speed (m/min)	Weld Width (mm)
1 (2) #	1	1.4	0.3	0.9
2 (2) #	1	1.6	0.4	1.0
3 (2) #	1	1.8	0.5	1.2
4 (2) #	1	2	0.6	1.4

Table 5. Cont.

Test Number	Defocusing Amount (mm)	Power (kW)	Welding Speed (m/min)	Weld Width (mm)
5 (2) #	0.5	1.4	0.4	0.7
6 (2) #	0.5	1.6	0.3	1.1
7 (2) #	0.5	1.8	0.6	1.1
8 (2) #	0.5	2	0.5	1.3
9 (2) #	0	1.4	0.5	0.7
10 (2) #	0	1.6	0.6	0.9
11 (2) #	0	1.8	0.3	1.3
12 (2) #	0	2	0.4	1.6
13 (2) #	−0.5	1.4	0.6	0.7
14 (2) #	−0.5	1.6	0.5	0.8
15 (2) #	−0.5	1.8	0.4	1.2
16 (2) #	−0.5	2	0.3	2.0
k1	1.125	0.750	1.325	-
k2	1.050	0.950	1.125	-
k3	1.125	1.200	1.000	-
k4	1.175	1.575	1.025	-
R	0.125	0.825	0.325	-

By further comparatively analyzing the relationships between different factors and levels and the k index (Figure 4), the influence of the defocusing amount, power, and welding speed on the weld width were obtained. The weld width decreased at first, and then increased with the growth of the defocusing amount (Figure 4a); both negative and positive defocusing amounts increased the weld width; the weld width was also always enlarged with the growing welding power (Figure 4b); moreover, the higher the power, the larger the growth rate of the weld width (as evinced by the rising slope of the curve in Figure 4b); finally an increase of the welding speed corresponded to a reduction at first, and then a slight growth of the weld width (Figure 4c).

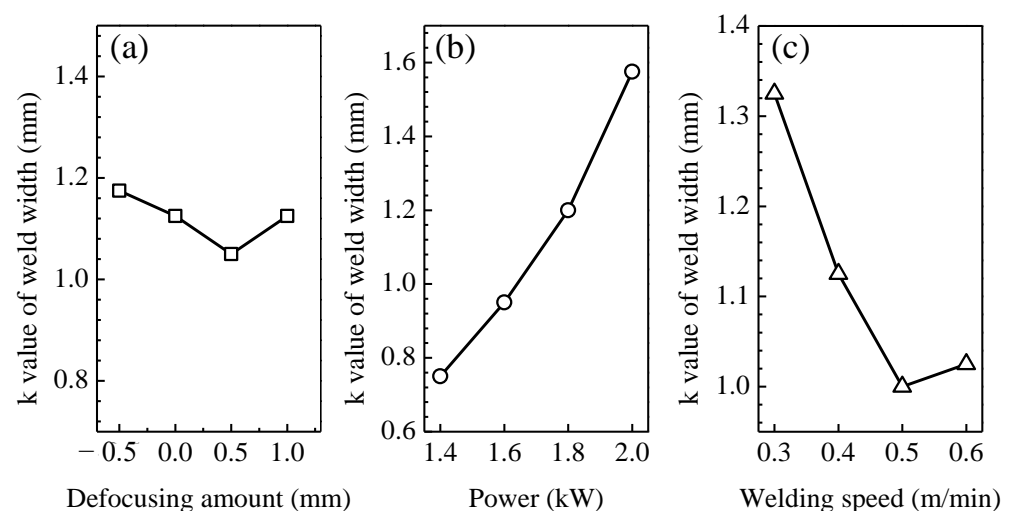


Figure 4. Relationships of (a) the defocusing amount, (b) power, and (c) welding speed with the weld width of Mo–Re joints with a thickness of 2 mm.

A metallographic observation was made on the cross sections of the joints with a thickness of 2 mm, through a three-factor and four-level orthogonal test, and the results are shown in Figure 5. At first, large-sized pores appeared in the FZ of some of the joints. According to research by Liu et al. [22], the type of pores were processing pores, which are induced by inappropriate welding parameters. Secondly, the grains in the FZ were all bulky columnar grains, and the grain size was obviously larger than that in the BM under different welding parameters. Finally, the heights of the reinforcements of the joints were all low under different welding parameters. Figure 6 is a macromorphology photo of the upper surface of the Mo–Re welding joints with a thickness of 2 mm. At first, transverse cracks were present in the joints, using parameters 6 (2) # and 7 (2) #, and no cracks occurred in the joints when using the other welding parameters. Secondly, the weld widths of the joints when using parameters 4 (2) #, 8 (2) #, 12 (2) # and 16 (2) # were remarkably larger than those obtained using the other parameters. Through further analysis, it was found that the welding power of the four joints were all equivalent to the maximum output power (2 kW) of the laser. Finally, the surfaces of the joints (except for the joints welded using parameters 4 (2) #, 8 (2) #, 12 (2) # and 16 (2) #) exhibited uneven waviness, showing poor forming quality.

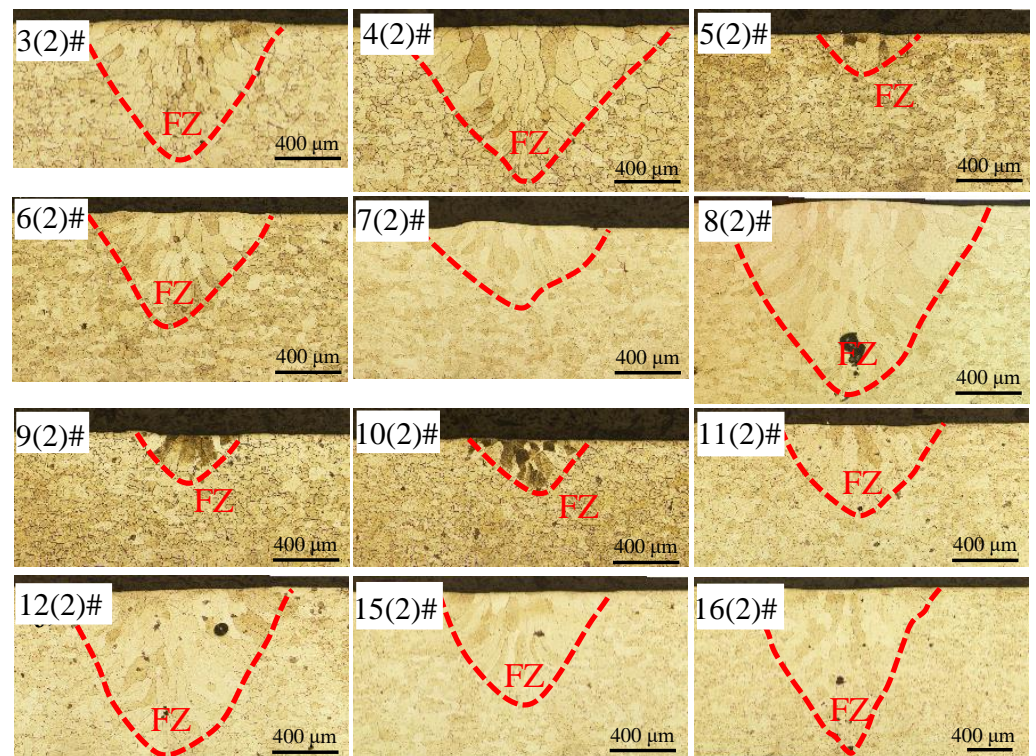


Figure 5. The metallographs of the cross sections of the Mo–Re joints with a thickness of 2 mm, obtained through a three-factor and four-level orthogonal test.

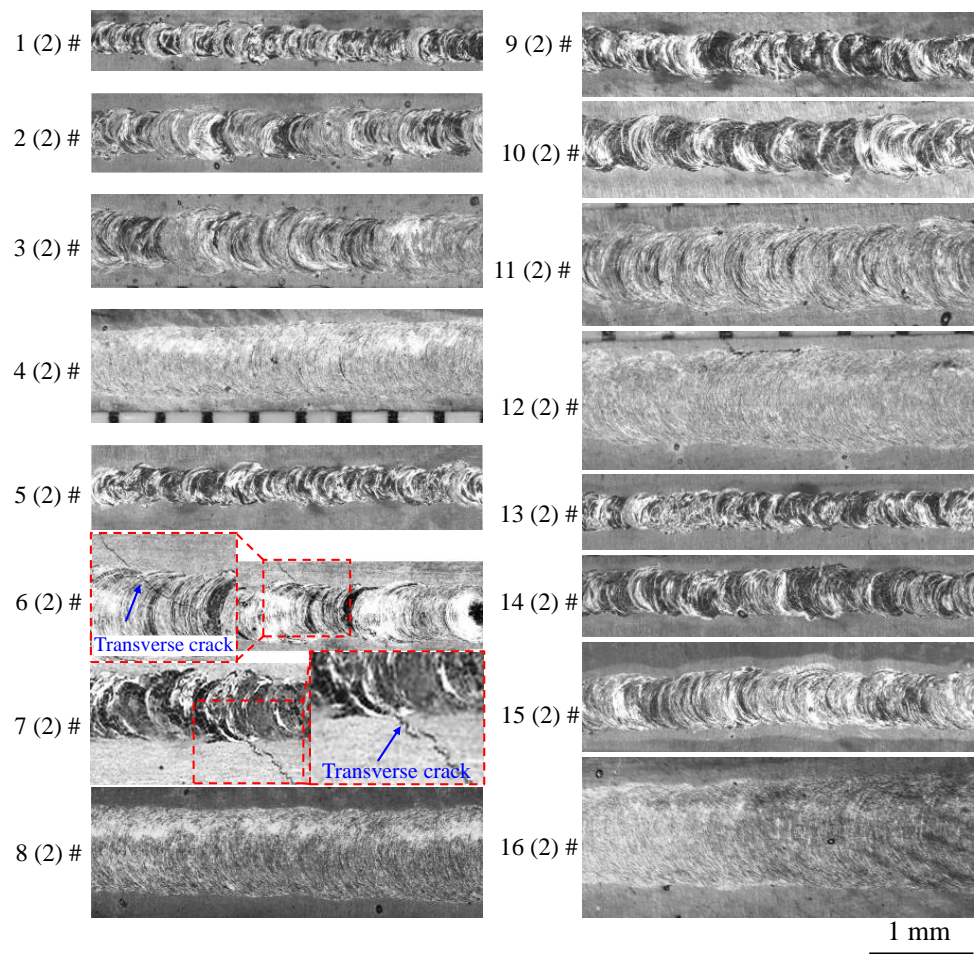


Figure 6. Macroscopic morphologies of the upper surface of the Mo–Re welding joints with a thickness of 2 mm.

3.2. The Influence Law of Welding Parameters on Properties and Microstructures of the Joints with the Thickness of 0.5 mm

A tensile test was performed on the Mo–Re joints with a thickness of 0.5 mm, and the results are shown in Figure 7. The maximum tensile strength (245.0 MPa) of the joint welded using the parameters 7 (0.5) # in the orthogonal test was the highest, in which the defocusing amount was 0 mm, the power was 1.7 kW, and the welding speed was 2 m/min. The joint welded using parameter 5 (0.5) #, i.e., a defocusing amount of 0.5 mm, a power of 1.7 kW, and a welding speed of 4 m/min, delivered the lowest maximum tensile strength (64.5 MPa). The largest tensile strength (245 MPa) of the joints obtained during the orthogonal test was also lower than that of the BM. The values of R corresponding to the laser power, the defocusing amount, and the welding speed were successively lowered (Table 6). This indicates that the welding power and the welding speed separately showed the most and least remarkable influences on the tensile strength. At a defocusing amount of 0.5~1.0 mm, the maximum tensile strengths of the joints rose with the growth of the defocusing amount, as shown in Figure 8a. At a power of 1.3~2.0 kW, the maximum tensile strengths of the joints dropped as the power increased, as shown in Figure 8b. At a welding speed of 2.0~3.0 m/min, the maximum tensile strengths of the joints slowly grew at first, and then rapidly decreased with an increase in the welding speed, as shown in Figure 8c. Furthermore, the Vickers hardness of the different zones of the cross sections of joints were measured, as shown in Figure 9. At first, no obvious differences were found in the hardness of the BM, HAZ, or FZ in the same joint; afterwards, the hardness of the same zone of the

joints obtained under different welding parameters also presented no significant difference. The average Vickers hardness of the different zones of the joints equaled 200 HV.

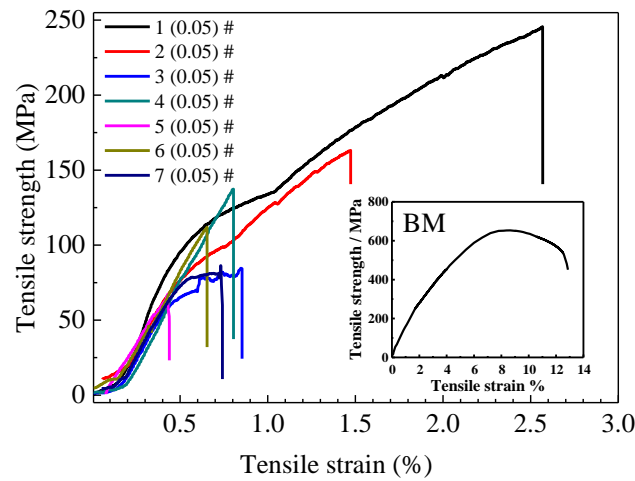


Figure 7. The stress–displacement curves of the Mo–Re welded joints with a thickness of 0.5 mm.

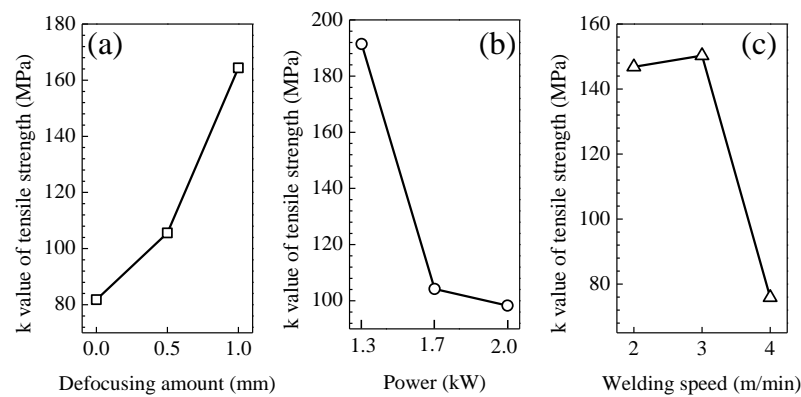


Figure 8. The relationships of (a) the defocusing amount, (b) power, and (c) welding speed with the maximum tensile strengths of the Mo–Re joints with a thickness of 0.5 mm.

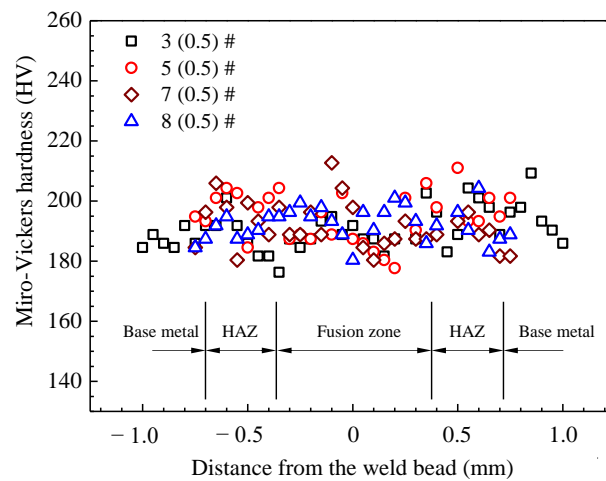


Figure 9. The hardness distribution of cross sections of the Mo–Re joints with a thickness of 0.5 mm.

Table 6. Analysis results of the maximum tensile strengths of the Mo–Re welded joints with a thickness of 0.5 mm, obtained through a three-factor and three-level orthogonal test.

Test Number	Defocusing Amount (mm)	Power (kW)	Welding Speed (m/min)	Tensile Strength MPa
1 (0.5) #	1	1.4	2	245.5
2 (0.5) #	1	1.7	3	163.3
3 (0.5) #	1	2	4	84.4
4 (0.5) #	0.5	1.4	3	137.3
5 (0.5) #	0.5	1.7	4	67.4
6 (0.5) #	0.5	2	2	112.1
7 (0.5) #	0	1.7	2	81.8
8 (0.5) #	0	2	3	-
9 (0.5) #	0	1.4	4	-
k1	164.4	191.4	146.8	-
k2	105.6	104.2	150.3	-
k3	81.8	98.3	75.9	-
R	82.6	93.2	74.4	-

The metallographic structures of the cross section of the joint (7 (0.5) #) with the largest maximum tensile strength were further observed (Figure 10). The microstructure in the FZ was coarse columnar grain, and those in the HAZ and the BM were coarse equiaxed grains. The coarse columnar grains in the FZ were mainly formed by melting the BM and then by crystallization events during the welding. The coarsening of the Mo grain greatly weakens the strength of the welded joints [23,24].

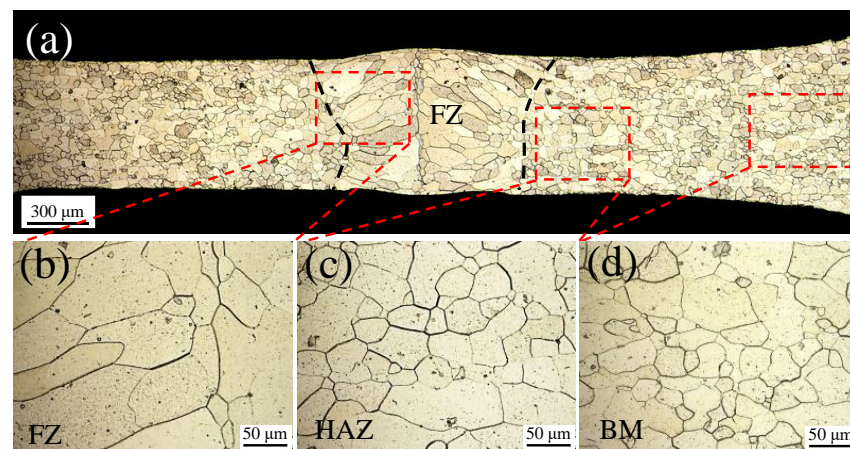


Figure 10. (a) Metallographic picture of the cross section of the joint welded using parameters 7 (0.5) #; (b–d) Magnified pictures of the FZ, HAZ, and BM, respectively.

The content and distribution of Re in the cross section of the joint were analyzed via an energy dispersive spectrometer (EDS). At first, the results of the area analysis and line scanning (Figure 11) showed that the content of Re in the FZ had no obvious difference compared to that in the HAZ and the BM, as shown in Figure 11d. The distribution of Re was uniform in the FZ, without significant macroscopic segregation (Figure 11c). Afterwards, an EDS point analysis was performed in different zones of the joint. The specific measurement positions were marked in Figure 12, and the measurement results are shown in Table 7. The average contents of Re in the FZ, HAZ, and BM were 4.03 wt.%, 3.39 wt.%, and 4.23 wt.%, respectively. Compared to the BM, the content of Re in the FZ did not remarkably decrease. This indicates that no obvious burning loss occurred to Re during the welding, which was mainly attributed to the fairly high melting point of Re (the melting points of Re and Mo are 3180 °C and 2670 °C, respectively).

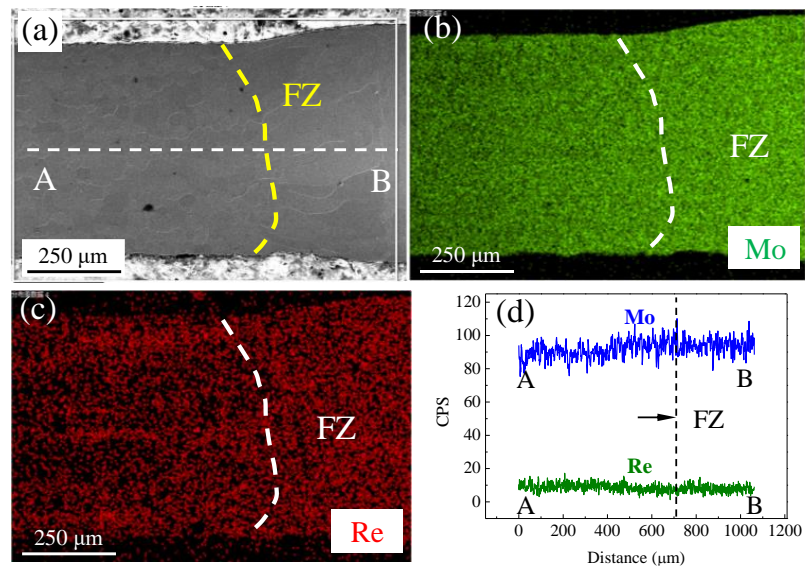


Figure 11. Result of EDS on the cross section of the joint welded using parameters 7 (0.5) #; (a) SEM image of the cross section; (b) the result of EDS area analysis of Mo; (c) the result of EDS area analysis of Re; (d) the result of EDS line scanning of Mo and Re along line AB in (a).

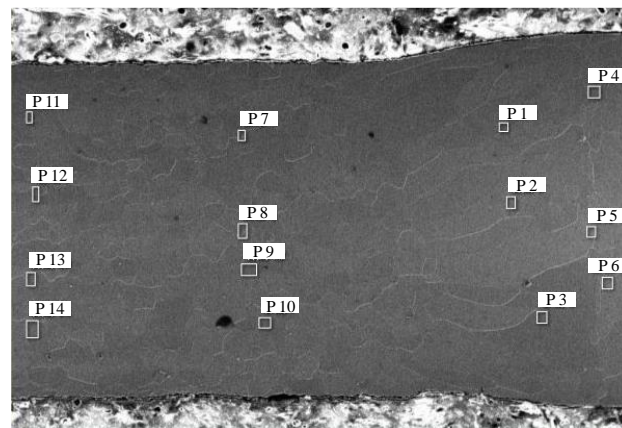


Figure 12. The measurement positions of the EDS point analysis on the cross section of the joint welded according to parameter (7 (0.5) #), P1–P14 indicates the sequence of EDS measurement positions and the white box indicates the EDS measurement position.

Table 7. EDS results of point analysis on the cross section of the joint (7 (0.5) #) in Figure 12.

Position	Test No.	Elements (wt.%)			
		Mo	Re	C	O
FZ	1	85.07	3.71	8.3	2.92
	2	82.76	4.03	10.75	2.45
	3	84.04	4.5	9.69	1.77
	4	81.39	3.41	11.88	3.32
	5	83.56	4.62	9.18	2.64
	6	86.33	3.9	7.64	2.12
	Average	83.86	4.03	9.57	2.54

Table 7. Cont.

Position	Test No.	Elements (wt.%)			
		Mo	Re	C	O
HAZ	7	79.22	4.18	11.84	4.76
	8	85.33	4.38	8.31	1.99
	9	86.28	3.19	7.9	2.63
	10	86.08	3.8	7.83	2.29
	Average	84.23	3.90	8.97	2.92
BM	11	83.29	4.95	11.76	0
	12	79.4	4.14	12.6	3.86
	13	83.87	4.46	9.5	2.46
	14	82.64	3.38	10.53	3.54
	Average	82.30	4.23	11.10	2.47

4. Discussion

Re in the BM of the Mo–Re alloy exists in the form of a solid solution, which greatly improves the ductility of the BM and reduces the DBTT. Therefore, it is necessary to analyze the existence and distribution modes of Re in the FZ of the welded joints, in order to attain the influencing mechanism and law of Re on the weldability of the joints.

The Effect of the Existence Modes of Re on the Properties of the Joints

At first, the existence modes of Mo and Re in the BM and FZ were analyzed using XPS, as shown in Figure 13. The peak-fitting result (Figure 13a) of the Mo 3d peak shows that apart from atomic Mo, Mo in the FZ also existed as Mo₂C and MoO₂, in which case, MoO₂ greatly weakened the bonding strength of the grain boundary [17]. The influence of Mo₂C on the strength of the grain boundary depends on the content and distribution pattern of the phase. Excessive Mo₂C is precipitated at the grain boundary in a network shape, which increases the brittleness of the grain boundary [25]. According to the corresponding areas of Mo elements with different chemical valence states in Figure 13a, it is feasible to analyze the relative contents of various phases at measurement positions (semi-quantitative result) [26]. The results showed that the contents of Mo atoms, Mo²⁺ (Mo₂C), and Mo⁴⁺ (MoO₂) were 52.00 at.%, 13.15 at.%, and 34.85 at.%, respectively. A certain amount of MoO₂ was distributed in the FZ, which certainly decreased the joint strength.

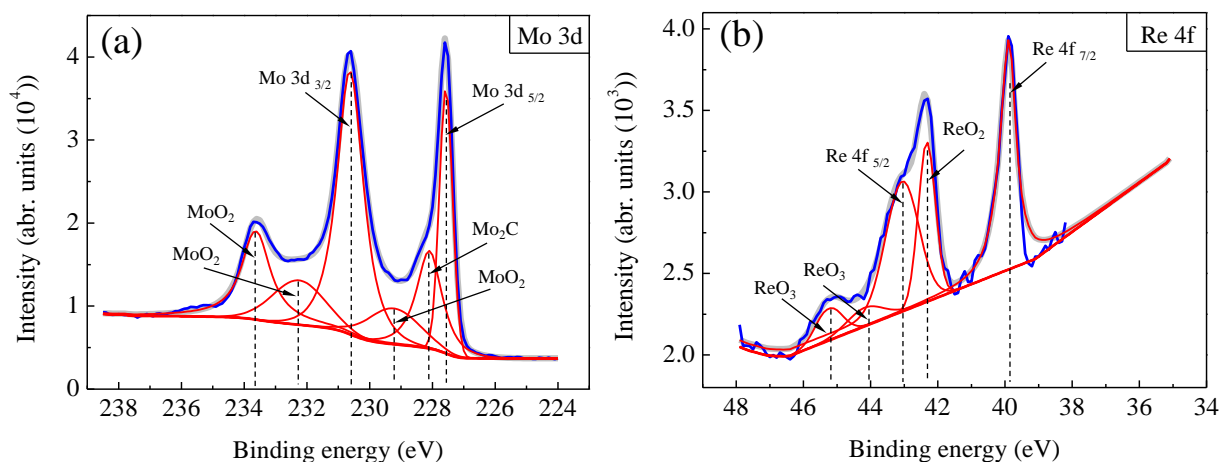


Figure 13. XPS results of Mo and Re elements: peak-fitting results of (a) Mo 3d and (b) Re 4f. The red curve indicates the spectrum of the phase used for the fitting, the blue curve indicates the fitted Mo3d spectrum and the gray curve indicates the original Mo3d spectrum.

The peak-fitting result (Figure 13b) of the Re 4f peak indicated that Re elements in the FZ are also present as rhenium oxides, in addition to Re atoms. According to the corresponding areas of Re with different chemical valence states in Figure 13b, it was possible to analyze the relative contents of Re atoms, Re^{3+} (ReO_3), and Re^{4+} (ReO_2) at the measurement positions (a semi-quantitative result). The results showed that the contents of the Re atoms, Re^{3+} (ReO_3) and Re^{4+} (ReO_2), were 73.67 at.%, 9.31 at.%, and 17.02 at.%, respectively. On one hand, the presence of rhenium oxides decreases the content of free O in the FZ of the joints, which is in favor of improving the bonding strength of the Mo grain boundary; on the other hand, it declines the content of the Re atoms, thus lowering the solid solution strengthening effect of Re in Mo.

Afterwards, the distribution of phases in the FZ and BM was analyzed using EBSD, to reveal the phase change and distribution law of the Re elements, as shown in Figure 14. At first, Figure 14b shows that the ReC phases (yellow particles) were distributed in the BM; moreover, the phases were also distributed at the Mo grain boundary and in grains while being relatively non-uniform, showing a certain degree of segregation; in addition, the relative contents of the ReC phases were relatively low and the remaining Re was distributed in its atomic state in the BM (Figure 11c). Furthermore, the phase distribution of Re in the FZ was analyzed (Figure 14d). It was found that apart from the ReC phases (yellow particles), there were also MoO_2 (red particles) and ReO_3 (blue particles) phases in the FZ (Figure 14d). Compared to the BM, the ReC was more uniformly distributed in the FZ. Many MoO_2 were distributed in the FZ and they tended to be distributed along the Mo grain boundary. Some ReO_3 phases were also found near the grain boundary.

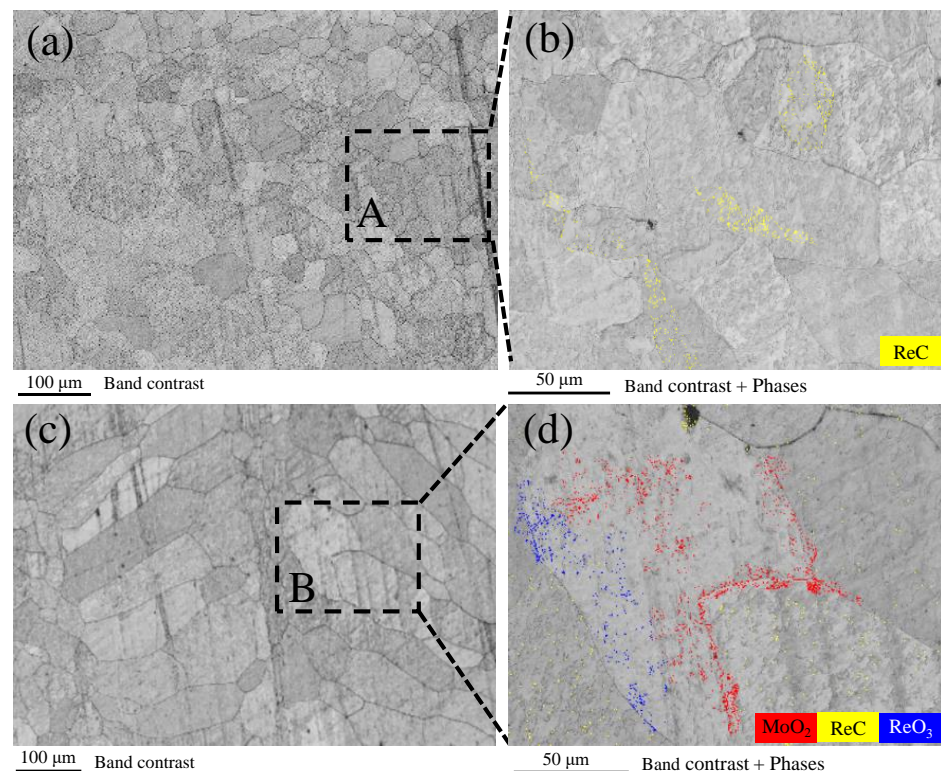


Figure 14. EBSD results in the BM and FZ of the Mo–Re alloy: (a) the band-contrast image of the BM; (b) the phase-distribution image of the A zone in the BM; (c) the band-contrast image of the FZ; (d) the phase-distribution image of the B zone in the FZ.

ReO_2 and ReO_3 phases that have precipitated in the FZ of the joint decrease the relative content of Re atoms and weaken the solid solution, strengthening the effect of Re to Mo. However, the precipitation of the ReO_2 and ReO_3 phases lowers the content of free O in the FZ and purifies the Mo grain boundary to some extent, which is beneficial for increasing

the bonding strength of the Mo grain boundary. Liu et al. [11] suggested that excessive rhenium oxides can enhance the brittleness of the joints. Moreover, ReO_2 (900 °C) and ReO_3 (400 °C) phases have relatively low decomposition temperatures, and inevitably affect the high-temperature strength of joints when the joints are in service at a high temperature. Therefore, the precipitation of ReO_2 and ReO_3 phases presents a two-sided effect on the strength of the FZ of the joints; it is extremely important to reasonably control the precipitation quantity of the ReO_2 and ReO_3 phases for improving the joint strength.

A large number of MoO_2 phases are found in the FZ. The phases greatly weaken the bonding strength of the grain boundary and reduce the tensile strength of the joints. The main reason for this is that MoO_2 easily epitaxially grows on the (110) crystal face of Mo (that is, (110)Mo/(010) MoO_2), thus forming a Mo-O-Mo sandwich structure [17,27]. The O in the sandwich structure appears at the grain boundary in the form of monolayers, which significantly declines the bonding strength of the two phases [17]. Many research results show that the more significant the segregation of O, the higher the brittleness of the Mo grain boundary and the lower the bonding strength [28].

The mean value of the maximum tensile strengths of the joints equals 127.3 MPa, which basically coincides with the maximum tensile strength of the joint for pure Mo [29]. This indicates that 5 wt.% of Re in the FZ fails to effectively improve the strength of Mo joints—that is, the Re elements of the content do not effectively reduce the weakening effect of O on the Mo grain boundary.

5. Conclusions

By employing a single-mode fiber laser, the effects of welding parameters on the mechanical properties of the joints were analyzed, based on an orthogonal test. Moreover, the existence modes of Re in the FZ were further analyzed through XPS and EBSD. The main conclusions are drawn as follows:

- The orthogonal test reveals that laser power has the most significant effect on the penetration and weld width of Mo–Re joints, and that the penetration and width monotonically rise with the growth of the power; the defocusing amount has the least remarkable influence on the penetration and weld width.
- The maximum and average tensile strengths of the Mo–Re joints are 250 MPa and 127.3 MPa, respectively; the micro-Vickers hardness distribution in the FZ, HAZ, and BM are all within 180~205 HV, and no obvious hardening phenomenon appears in the FZ.
- The microstructure in the FZ of the Mo–Re joints consists of coarsening columnar grains, while that in the HAZ corresponds to equiaxed grains. The EDS result indicates that there is no significant macroscopic segregation of Re in the FZ. Apart from its atomic state, Re in the FZ also exists as ReO_2 , ReO_3 , and ReC.

Author Contributions: Conceptualization, L.-J.Z. and L.-L.Z.; methodology, L.-L.Z., Q.-J.Y. and L.-J.Z.; validation, L.-L.Z. and Q.-J.Y.; data curation, Q.-J.Y.; writing—original draft preparation, L.-L.Z.; writing—review and editing, L.-L.Z. and L.-J.Z.; visualization, L.-L.Z.; supervision, L.-J.Z.; funding acquisition, L.-J.Z. All authors have read and agreed to the published version of the manuscript.

Funding: This work was supported by the National Natural Science Foundation of P.R. China (Grant No. 51775416), the Major Project of Advanced Metal Materials Science and Technology of Shaanxi Province (Grant No. 2020ZDZX04-02-01), and the Project of Innovation Team of Xi'an Jiaotong University (Grant No. XTR0118008).

Institutional Review Board Statement: Not applicable.

Informed Consent Statement: Not applicable.

Data Availability Statement: Data sharing is not applicable.

Acknowledgments: The authors would thank the engineers at the Instrument Analysis Center of Xi'an Jiaotong University for their assistance with XPS, SEM, EBSD, and TEM analyses. The Jinduicheng Molybdenum Group Co., LTD is thanked for providing the material.

Conflicts of Interest: The authors declare no conflict of interest.

References

1. Zinkle, S.J. Materials challenges in nuclear energy. *Acta Mater.* **2013**, *61*, 735–758. [[CrossRef](#)]
2. Zhu, Q.; Xie, M.; Shang, X.; An, G.; Sun, J.; Wang, N.; Xi, S.; Bu, C.; Zhang, J. Research status and progress of welding technologies for molybdenum and molybdenum alloys. *Metals* **2020**, *10*, 279. [[CrossRef](#)]
3. Huang, H.; Wang, W.; Zhong, W.; Zheng, J.; Zhao, S. Research Progress on Application of Mo-Re Alloy in Space Nuclear Power. *At. Energy Sci. Technol.* **2020**, *54*, 505.
4. Hiraoka, Y.; Morito, F.; Okada, M.; Watanabe, R. Effect of a small amount of additional carbon on the ductility of recrystallized sintered-molybdenum sheet. *J. Nucl. Mater.* **1978**, *78*, 192–200. [[CrossRef](#)]
5. Hiraoka, Y.; Okada, M.; Watanabe, R. Effect of aging after carbon doping on the ductility of molybdenum. *J. Less-Common Met.* **1980**, *75*, 31–42. [[CrossRef](#)]
6. Klopp, W.D.; Witzke, W.R. Mechanical properties of electron-beam-melted molybdenum and dilute molybdenum-rhenium alloys. *Metall. Trans.* **1972**, *4*, 2006–2008. [[CrossRef](#)]
7. Hiraoka, Y.; Okada, M.; Irie, H. Alloying to improve the properties of welded molybdenum. *J. Nucl. Mater.* **1988**, *155*, 381–385. [[CrossRef](#)]
8. Morgunova, N.N.; Abramyan, A.V.; Kazakova, N.I. Effect of rhenium on the brittle fracture threshold of molybdenum. *Met. Sci. Heat Treat.* **1987**, *29*, 441–447. [[CrossRef](#)]
9. Burkhanov, G.S.; Yusupov, V.S.; Roschupkin, V.V.; Karelin, F.R.; Kirillova, V.M.; Karelin, R.D.; Ermishkin, V.A.; Minina, N.A.; Sdobyrev, V.V.; Serebryany, V.N.; et al. Manufacturing features, structure, and properties of high-purity Mo-Re thin sheets. *J. Phys. Conf. Ser.* **2021**, *1758*, 012006. [[CrossRef](#)]
10. Zhang, Y.; Wang, T.; Jiang, S.; Zhang, B.; Yong, W.; Feng, J. Effect of rhenium content on microstructures and mechanical properties of electron beam welded TZM alloy joints. *J. Manuf. Process.* **2018**, *32*, 337–343. [[CrossRef](#)]
11. Peng, L.; Feng, K.Y.; Zhang, G.M. A novel study on laser lap welding of refractory alloy 50Mo–50Re of small-scale thin sheet. *Vacuum* **2017**, *136*, 10–13.
12. Olds, L.E.; Rengstorff, G.W.P. Effects of Oxygen, Nitrogen, and Carbon on The Ductility of Cast Molybdenum. *JOM* **1956**, *8*, 150–155. [[CrossRef](#)]
13. Babinsky, K.; Weidow, J.; Knabl, W.; Lorich, A.; Leitner, H.; Primig, S. Atom probe study of grain boundary segregation in technically pure molybdenum. *Mater. Charact.* **2014**, *87*, 95–103. [[CrossRef](#)]
14. Janisch, R.; Elsässer, C. Segregated Light Elements at Grain Boundaries in Niobium and Molybdenum. *Phys. Rev. B* **2003**, *67*, 2209–2219. [[CrossRef](#)]
15. Kurishita, H.; Tokunaga, O.; Yoshinaga, H. Effect of Nitrogen on the Intergranular Brittleness in Molybdenum. *Mater. Trans.* **2007**, *30*, 1009–1015. [[CrossRef](#)]
16. Leitner, K.; Lutz, D.; Knabl, W.; Eidenberger-Schober, M.; Huber, K.; Lorich, A.; Clemens, H.; Maier-Kiener, V. Grain boundary segregation engineering in as-sintered molybdenum for improved ductility. *Scr. Mater.* **2018**, *156*, 60–63. [[CrossRef](#)]
17. Krajnikov, A.V.; Drachinskiy, A.S.; Slyunyaev, V.N. Grain boundary segregation in recrystallized molybdenum alloys and its effect on brittle intergranular fracture. *Int. J. Refract. Met. Hard Mater.* **1992**, *11*, 175–180. [[CrossRef](#)]
18. Hughes, G.G.J. The alloys of rhenium with molybdenum or with tungsten and having good high-temperature properties. In *Plansee Proceedings*; Pergamon Press: London, UK, 1955.
19. Kramer, D.P.; Mcdougal, J.R.; Booher, B.A.; Ruhkamp, J.D. Electron beam and Nd-YAG laser welding of niobium-1% zirconium and molybdenum-44.5% rhenium thin select material. *Energy Convers. Eng. Conf. Exhib.* **2013**, *2*, 956–961.
20. Matsuda, F.; Nakata, K.; Mandokoro, Y. Effect of Rhenium and Niobium on Weld Metal Ductility of Molybdenum by EB Welding. *Trans. JWRI* **1984**, *13*, 255–261.
21. Morito, F. Characteristics of EB-weldable molybdenum and Mo-Re alloys. *JOM* **1993**, *45*, 54–58. [[CrossRef](#)]
22. Zhang, L.J.; Liu, J.Z.; Pei, J.Y.; Ning, J.; Zhang, L.L.; Long, J.; Zhang, G.F.; Zhang, J.X.; Na, S.J. Effects of Power Modulation, Multipass Remelting and Zr Addition Upon Porosity Defects in Laser Seal Welding of End Plug to Thin-Walled Molybdenum Alloy. *J. Manuf. Process.* **2019**, *41*, 197–207. [[CrossRef](#)]
23. Wronski, A.; Chilton, A.; Capron, E. The ductile-brittle transition in polycrystalline molybdenum. *Acta Metall.* **1969**, *17*, 751–755. [[CrossRef](#)]
24. Wadsworth, J.; Morse, G.R.; Chewey, P.M. The microstructure and mechanical properties of a welded molybdenum alloy. *Mater. Sci. Eng.* **1983**, *59*, 257–273. [[CrossRef](#)]
25. Zhang, L.-L.; Zhang, L.-J.; Long, J.; Ding, X.-D.; Sun, J.; Sun, Y.-J. Improvement in the weldability of molybdenum alloy by pre-welding solid carburizing. *J. Mater. Sci. Technol.* **2020**, *80*, 1–12. [[CrossRef](#)]
26. Watts, J.F.; Wolstenholme, J. *An Introduction to Surface Analysis by XPS and AES*, 2nd ed.; John Wiley & Sons Ltd.: Hoboken, NJ, USA, 2019.

27. Magneli, A.; Andersson, G. On the MoO₂ structure type. *Acta Chem. Scand.* **1955**, *9*, 1378–1381. [[CrossRef](#)]
28. Zelenskii, G.K.; Borodich, V.D.; Korontsevich, V.K.; Milovidov, S.N.; Filkin, V.Y. Effect of purity on the structure and properties of molybdenum. *Met. Sci. Heat Treat.* **1972**, *14*, 22–25. [[CrossRef](#)]
29. Zhang, L.-L.; Zhang, L.-J.; Long, J.; Sun, X.; Zhang, J.-X.; Na, S.-J. Enhanced mechanical performance of fusion zone in laser beam welding joint of molybdenum alloy due to solid carburizing. *Mater. Des.* **2019**, *181*, 1–12. [[CrossRef](#)]